Nano Research Energy

ISSN 2791-0091 (print); 2790-8119 (online)
https://doi.org/10.26599/NRE.2026.9120239

Research Article

Sulfonate-grafted graphene separators enabling electrostatic regulation of Li^+ desolvation and transport in lithium metal batteries

Yuanyuan Luo[1], Yuluo Chen[1], Mingfeng Tan[2], Helei Wei[2] (✉), Bo Lin[2] (✉), and Henghui Xu[1] (✉)

[1] *State Key Laboratory of New Textile Materials and Advanced Processing, School of Materials Science and Engineering, Huazhong University of Science and Technology, Wuhan 430074, China*
[2] *Global R & D Center, Guangxi Liugong Metathings Technology Co., Ltd., Liuzhou 545007, China*

Received: 11 February 2026 / **Revised:** 18 April 2026 / **Accepted:** 27 April 2026 / **Published date:** 23 June 2026

ABSTRACT

In lithium metal batteries, sluggish Li^+ desolvation and anion-dominated ion transport at the separator–electrolyte interface fundamentally limits interfacial kinetics and trigger unstable lithium deposition. Lithium metal batteries suffer from slow interfacial kinetics and unstable lithium deposition, due to poor Li^+ desolvation and uncontrolled anion transmittance at the separator–electrolyte interface. Here, a sulfonate-functionalized graphene was coated onto a polypropylene (PP) separators to construct an intrinsic anionic electrostatic field layer, which simultaneously regulates ion transport and promotes interfacial desolvation. This negatively charged field not only repels anions but also reshapes the local solvation environment, thereby facilitating Li^+ desolvation and transport, leading to a high lithium-ion transference number of 0.79. Meanwhile, the negatively charged interface repels polarized solvent molecules and redistributes local electric field lines, weakening Li^+-solvent charge–dipole interactions and lowering the Li^+ desolvation energy barrier, thereby accelerating Li^+ transport kinetics. Benefiting from homogenized Li^+ flux and facilitated desolvation, the modified separator enables uniform lithium deposition and effectively suppresses dendrite growth, allowing Li symmetric cells to cycle stably for over 1000 h with low polarization. In full cells, Li||NCM622 batteries exhibit excellent high-voltage cycling stability, achieving 82% capacity retention after 1000 cycles, more than doubling that of cells using conventional PP separators. Moreover, Si–C||NCM811 pouch cells retain over 80% capacity after 700 cycles at 1C, demonstrating promising scalability and practical applicability.

KEYWORDS

lithium batteries, separators, functionalization, dendrite growth, conductivity

1 Introduction

Lithium metal anodes are widely regarded as the ultimate choice for next-generation rechargeable batteries owing to their ultrahigh theoretical capacity (3860 $mAh \cdot g^{-1}$) and the lowest electrochemical potential (–3.04 V vs. SHE) [1–5]. However, the practical application of lithium metal batteries (LMBs) remains severely hindered by large polarization, sluggish interfacial kinetics, and unstable lithium deposition, especially under high current density and high-voltage operation [6–10]. These challenges are closely related to ion transport and interfacial processes occurring at the separator/anode interface, where inefficient Li^+ transport amplifies concentration gradients and promotes dendritic lithium growth [11–14].

At the separator/anode interface, ion transport in conventional liquid electrolytes is typically dominated by mobile anions, while Li^+ migration is impeded by strong interactions with surrounding solvent molecules [15–17]. The desolvation of Li^+ requires breaking the charge–dipole interactions between Li^+ and solvent molecules in its solvation shell, which creates a kinetic bottleneck for interfacial Li^+ transport and intensifies concentration polarization during cycling [18–20]. To address these issues, separator surface engineering has been widely explored as a scalable strategy to regulate ion transport [21, 22]. Previous studies have shown that introducing negatively charged functional groups, such as carboxylate species, onto separator surfaces can repel free anions (e.g., PF_6^-), increase the lithium-ion transference number, and partially relieve concentration polarization [23–26]. However, such designs generally generate localized surface charges that are readily screened in liquid electrolytes, limiting their influence on solvent-coordinated Li^+ species and interfacial desolvation kinetics [27]. As a result, Li^+ desolvation at the separator interface is only indirectly affected, and the coupling

Address correspondence to Helei Wei, Weihelei@liugong.com; Bo Lin, linbo@liugong.com; Henghui Xu, xuhh@hust.edu.cn

between anion regulation and Li^+ desolvation remains underutilized.

Here, we report an electrostatic-field-driven separator design based on sulfonate-functionalized graphene coatings. By covalently anchoring immobile sulfonate (SO_3^-) groups onto a rigid graphene framework, a continuous and stable anionic electrostatic field is formed at the separator surface. This fixed electrostatic field simultaneously repels free PF_6^- anions and negatively polarized solvent molecules after solvation. As a result, the interaction between Li^+ and solvent molecules is likely weakened, leading to a reduced Li^+ desolvation energy barrier., and Li^+ becomes the dominant charge carrier. This effect is inferred from the enhanced Li^+ transport behavior observed in electrochemical measurements. yielding a high lithium-ion transference number of 0.79 (Scheme 1). This unified electrostatic regulation alleviates concentration polarization at the source, improves interfacial transport kinetics, and enables uniform lithium deposition while effectively suppressing dendrite growth. Consequently, Li||NCM cells exhibit excellent high-voltage cycling stability at 4.3 V and retain 82% capacity after 1000 cycles, which is approximately twice that of cells using pristine separators. Moreover, Si/C||NCM pouch cells operate stably for 700 cycles at 1C, demonstrating good compatibility with existing battery manufacturing, together with markedly improved Coulombic efficiency and thermal stability. You can simply type your text into this template or modify an already prepared manuscript based on the template formatting.

2 Results and discussion

Sulfonate-functionalized graphene was synthesized as an ionic conductive agent (ICA) by grafting lithiated sulfonic acid groups onto graphene sheets [28]. As shown in Fig. 1(a), graphene (Gr) shows a (002) peak at 25.4°, while ICA displays a pronounced shift to 22.7°, corresponding to a significantly expanded interlayer spacing. This peak shift reflects structural distortion induced by sulfonate functionalization, which provides a favorable structural basis for enhanced ion transport within the ICA framework. Raman spectroscopy was employed to probe structural disorder in the carbon framework (Fig. 1(b) and Fig. S1 in the Electronic Supplementary Material (ESM)). Both Gr and ICA display characteristic D and G bands at approximately 1350 and 1580 cm^{-1}, confirming their graphitic nature [29]. Compared with Gr, ICA shows an obvious change in the *D*/*G* feature after sulfonation, indicating modified defect density and local structural disorder induced by chemical grafting. Raman analysis reflects changes in the sp^2 carbon network, while the specific chemical nature of sulfonate grafting is further verified by Fourier transform infrared spectroscopy (FTIR). As shown in Fig. 1(c), ICA exhibits distinct absorption bands at 1207 and 1030 cm^{-1}, corresponding to the stretching vibrations of S=O and S-O bonds [30], respectively, confirming the successful introduction of sulfonate groups. Scanning electron microscopy (SEM) images of ICA (Fig. 1(d) and Fig. S2 in the ESM) reveal a spherical morphology at the micrometer scale with negligible agglomeration. Compared with Gr, ICA exhibits a smaller particle size, more regular morphology, and smoother surface, which is favorable for forming a uniform and compact coating on the separator. EDS elemental mapping (Fig. S3 in the ESM) shows a high content of O and S, confirming the successful introduction of sulfonate groups. The pristine PP separator displays a typical fibrous porous structure with uniformly distributed pores (Fig. S4(a) in the ESM). The ICA and Gr materials were evenly coated onto the PP separator, designated as PP+ICA and PP+Gr, respectively. ICA particles are homogeneously distributed on the PP surface without obvious agglomeration or peeling (Fig. 1(e)). In contrast, after coating with Gr, the separator surface shows irregular flake-like aggregates with partial coverage and local stacking (Fig. 1(f)), which may block membrane pores and lead to non-uniform ion transport pathways. Moreover, due to the absence of ion-selective suppresses anion migration and promotes Li^+ transport functional groups, graphene cannot effectively regulate ion transport behavior, which limits its ability to improve electrochemical performance. To further examine the coating structure, cross-sectional SEM images were obtained (Figs. S4(b)–S4(d) in the ESM). The PP+ICA separator shows a thin and uniform coating layer, while the PP+Gr separator exhibits a much thicker and less uniform layer, confirming the structural advantage of the ICA coating.

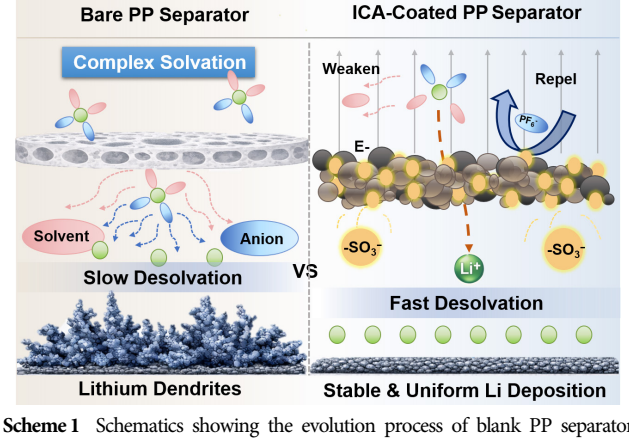

Scheme 1 Schematics showing the evolution process of blank PP separator and SO_3Li-modified PP separator during charging.

In addition to structural modification, ICA coating significantly improves the physical properties of the separator. The PP+ICA separator exhibits enhanced thermal stability and dimensional integrity at elevated temperatures compared with pristine PP (Fig. 1(g), Fig. S5 in the ESM), after heating at 120 and 150 °C, the PP+ICA separator maintains a significantly higher size retention compared with PP and PP+Gr, indicating its superior thermal stability. Thermogravimetric analysis revealed that the thermal stability of PP+ICA was the highest, further indicating an enhancement in the heat resistance of the modified separator (Fig. 1(h)). Moreover, electrolyte wettability is markedly improved after ICA modification. The contact angle decreases from 58.78° for PP to 22.16° for PP+ICA (Fig. 1(i)), indicating strong electrolyte affinity arising from the polar sulfonate groups. These structural and physicochemical characteristics establish the foundation for the electrostatic regulation of ion transport and Li^+ desolvation discussed in subsequent sections. Raman spectroscopy (Fig. S6(a) in the ESM) was performed to probe the electrolyte environment. Although no obvious peak shift is observed in the C=O stretching region, slight variations in peak intensity and spectral profile suggest a subtle change in the local coordination environment of Li^+–solvent interactions [31, 32]. To further clarify this effect, theoretical calculations were conducted. As shown in Figs. S6(b) and S6(c) in the ESM, the coordination distance between Li^+ and the carbonyl oxygen in EC increases from 1.822 to 1.966 Å after introducing sulfonate groups, indicating a weakened Li^+–solvent interaction. Meanwhile, the stronger interaction between Li^+ and the sulfonate-functionalized surface

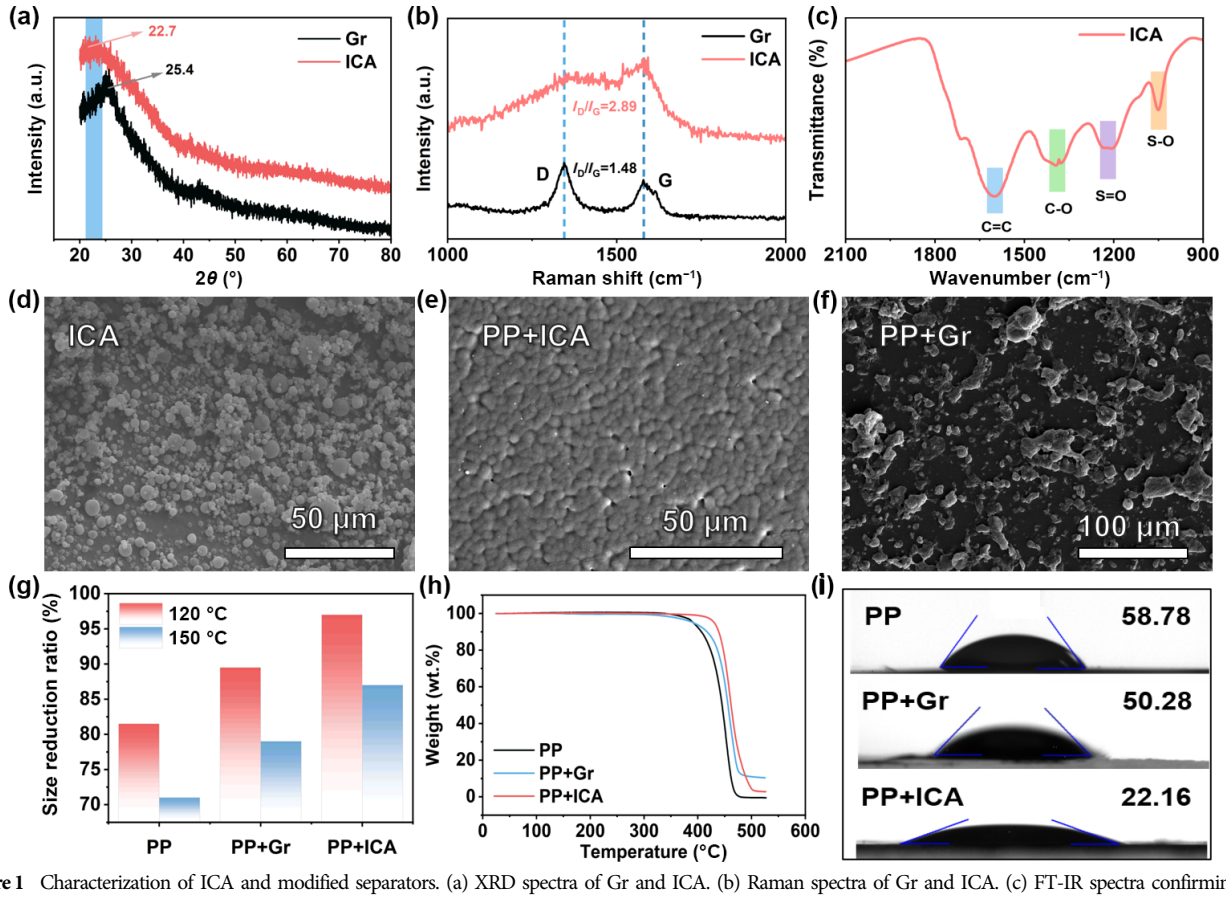

Figure 1 Characterization of ICA and modified separators. (a) XRD spectra of Gr and ICA. (b) Raman spectra of Gr and ICA. (c) FT-IR spectra confirming the introduction of sulfonate groups. (d) SEM image of ICA. (e, f) Surface SEM images of PP+ICA and PP+Gr separators. (g) Thermal shrinkage comparison of PP, PP+Gr, and PP+ICA after heating at 120 and 150 °C for 30 min. (h) Thermogravimetric analysis (TGA) curves of PP, PP+Gr, and PP+ICA. (i) Contact angle measurements showing the electrolyte wettability of different separators.

suggests that Li^+ is preferentially attracted to the fixed anionic sites. These results indicate that the ICA coating can modulate the local solvation structure and facilitate Li^+ desolvation.

Separator wettability and porosity strongly influence electrolyte uptake and Li^+ transport behavior. As shown in Fig. 2(a), pristine PP exhibits a porosity of 44.6% with an electrolyte absorption of 121%, while graphene modification (PP+Gr) increases the porosity to 52.2% through partial expansion of pore space. After ICA coating, the porosity further increases to 62.9%, accompanied by markedly enhanced electrolyte absorption. This enhancement can be mainly attributed to the relatively loose structure of the ICA coating, which introduces additional internal voids. Since the overall thickness and apparent volume of the separator change only slightly after coating, the increased pore volume leads to a higher porosity. In addition, the polar sulfonate groups in ICA further improve electrolyte affinity, contributing to the enhanced electrolyte uptake. The t_{Li^+} plays a crucial role in assessing ion transport efficiency, contributing to the mitigation of concentration polarization and the inhibition of lithium dendrite nucleation [33, 34]. The lithium-ion migration numbers of the three battery types were determined using the potentiostatic polarization method (Fig. 2(b) and Fig. S7 in the ESM). Notably, the lithium-ion transference number for PP+ICA was 0.79 (Fig. 2(c)), significantly surpassing both the blank PP separator (0.48) and the PP+Gr separator (0.42). This finding was corroborated by the exchange current density (I_0) associated with reaction kinetics (Fig. 2(d)). The I_0 value for PP+ICA stood at 0.262 mA·cm^{-2}, doubling the I_0 value of the blank PP separator at 0.127 mA·cm^{-2}, suggesting that the coating expedited the electrochemical reaction at the interface [35]. Electrochemical impedance spectroscopy (EIS) (Fig. S8 in the ESM) shows that surface coating inevitably introduces additional resistance to ion transport, with PP+ICA exhibiting a less pronounced impact compared to PP+Gr. This slight decrease in conductivity is mainly due to the suppressed mobility of anions, while the Li^+ transport is enhanced, leading to a higher lithium-ion transference number.

To clarify the influence of the ICA on interfacial redox kinetics, cyclic voltammetry measurements were conducted using symmetric cells (Fig. 2(e)). The PP+ICA separator exhibits more pronounced redox peaks with a peak current of 0.78 mA, exceeding that of pristine PP (0.63 mA), reflecting accelerated electrochemical reaction kinetics enabled by the modified separator interface. The effect of ICA on Li^+ transport behavior was further examined by CV tests at different scan rates (Fig. 2(f) and Fig. S9 in the ESM). Across the entire scan-rate range, PP+ICA consistently delivers higher current responses than PP and PP+Gr. During oxidation, the slope of the peak current for PP+ICA reaches 3.12, compared with 2.12 for pristine PP, indicating enhanced Li^+ transport and faster charge-transfer processes. Based on this analysis, the Li^+ diffusion coefficient was calculated, with PP+ICA achieving the highest value of 5.84×10^{-9} cm^2·s^{-1}), substantially higher than that of PP (2.46×10^{-9} cm^2·s^{-1}) (Fig. 2(g)). The lithium-ion diffusion coefficient of the battery was dynamically observed during charging and discharging using the galvanostatic intermittent titration technique (GITT) [36] (Fig. S10 in the ESM). During charging (Fig. 2(h)), the PP+ICA

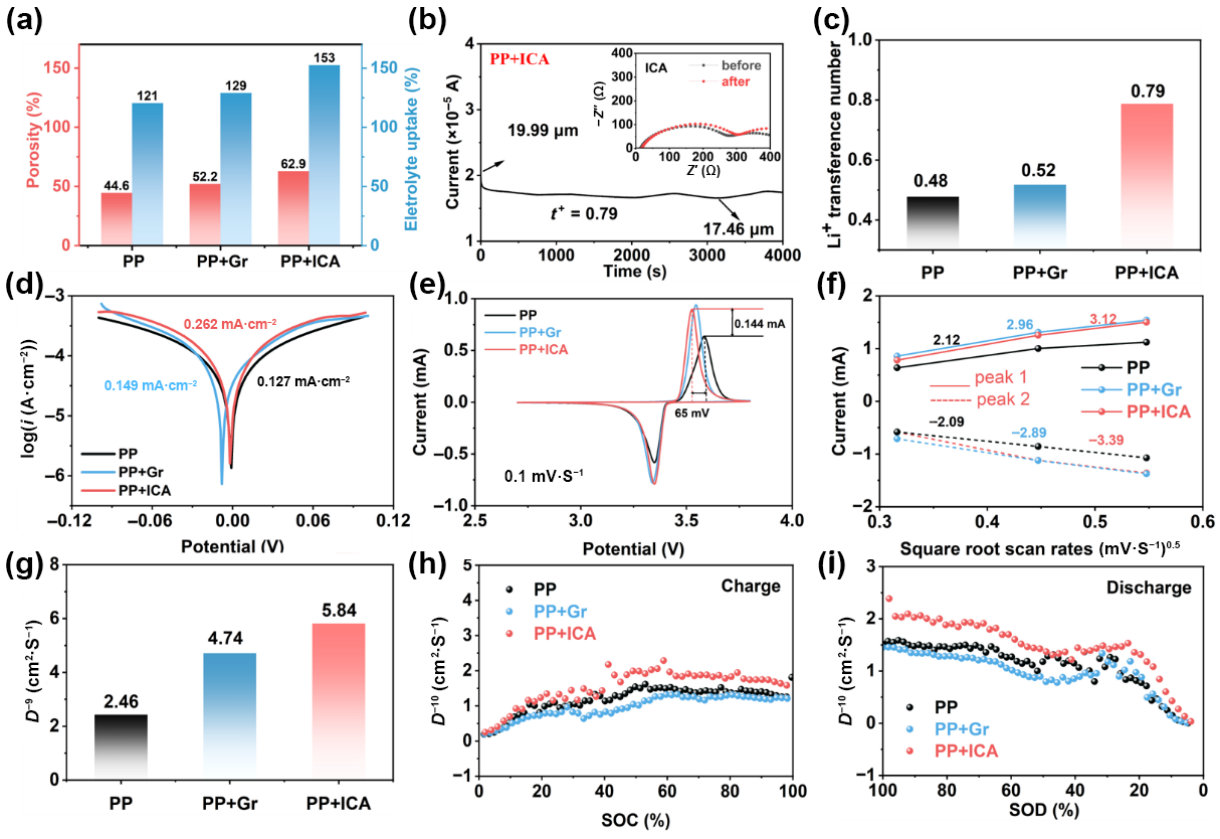

Figure 2 Ion transport properties of different separators. (a) Porosity and electrolyte uptake of PP, PP+Gr, and PP+ICA separators. (b) Chronoamperometry (*I*–*t*) curves and corresponding impedance spectra used for determining Li^+ transference number. (c) Calculated Li^+ transference numbers of different separators. (d) Tafel plots for Li plating/stripping kinetics in Li||Li symmetric cells. (e, f) Relationship between CV peak current and the square root of scan rate. (g–i) Li^+ diffusion coefficients derived from CV and GITT during overall, charging, and discharging processes, respectively, indicating enhanced Li^+ transport in PP+ICA.

separator exhibits a higher Li^+ diffusion coefficient over the entire state-of-charge range and during the discharge process (Fig. 2(i)), the PP+ICA separator consistently delivers a higher and more stable Li^+ diffusion coefficient, whereas the pristine PP separator exhibits a pronounced decay. This behavior is attributed to the fixed anionic electrostatic field introduced by sulfonate groups, which suppresses anion accumulation and weakens Li^+–solvent interactions at the interface, thereby facilitating sustained Li^+ transport during both charge and discharge. This electrostatic field regulates the local ion distribution near the interface, suppressing anion transport and enhancing Li^+ transport contribution.

To further confirm the impact of the enhanced Li^+ transport facilitated by the -SO_3Li group-modified ICA on the PP separator in enhancing the stability of the lithium metal anode interface, we assessed the electrochemical performance using Li-Cu batteries and Li-Li symmetric batteries. Coulombic efficiency (CE) serves as a crucial metric for assessing lithium utilization throughout cycling. Under a current density of 0.5 mA·cm^{-2}, the battery employing a PP+ICA separator demonstrates consistent cycling over 100 cycles, whereas the battery utilizing a pristine PP separator exhibits a rapid decline in CE after 60 cycles (Fig. 3(a)), demonstrating superior cycle life and enhanced lithium utilization due to the facilitation of Li^+ transfer by ICA. Additionally, ICA helps maintain a consistent Li^+ concentration on the anode surface, thereby impeding diffusion-driven lithium dendrite formation. A Li-Li symmetric cell was used to evaluate interfacial stability during resting (Fig. S11 in the ESM). Compared with pristine PP, the PP+ICA separator shows markedly suppressed impedance growth, indicating mitigated interfacial degradation. This behavior originates from the ICA-induced electrostatic field, which repels anions and solvent species, promotes Li^+-dominated transport, and stabilizes lithium deposition during resting. Under a current density of 1 mA·cm^{-2}, the polarization voltages of batteries assembled with blank PP, PP+Gr, and PP+ICA were tested (Fig. 3(b)). The symmetric cell assembled with pristine PP shows increasing voltage fluctuation after 400 h and fails at approximately 600 h due to uncontrolled lithium dendrite growth and internal short circuit. The PP+Gr-based cell exhibits instability at an earlier stage before 200 h, which is attributed to the intrinsically conductive nature of graphene and its nonselective ion transport behavior, leading to uneven ion distribution and unstable lithium deposition during cycling. In contrast, the PP+ICA-based symmetric cell operates steadily for more than 1200 h with a stable overpotential of approximately 24 mV. This outcome suggests that the ICA coating effectively controls Li^+ flow and enhances cycle performance.

To further assess the impact of ICA functional coatings on facilitating uniform lithium deposition, we conducted constant current charge-discharge tests on symmetrical cells at varying current densities (0.5–2 mA·cm^{-2}) and examined the surface morphology of the deposited lithium after disassembling the cycling batteries. With increasing current density, all cells exhibit a rise in overpotential accompanied by transient fluctuation, reflecting the kinetic response of the lithium deposition–dissolution process under elevated Li^+ flux demand (Fig. S12 in the ESM). The PP+ICA-based cell maintains the lowest and most stable overpotential throughout the test, indicating rapid interfacial adjustment and sustained Li^+ transport regulation under

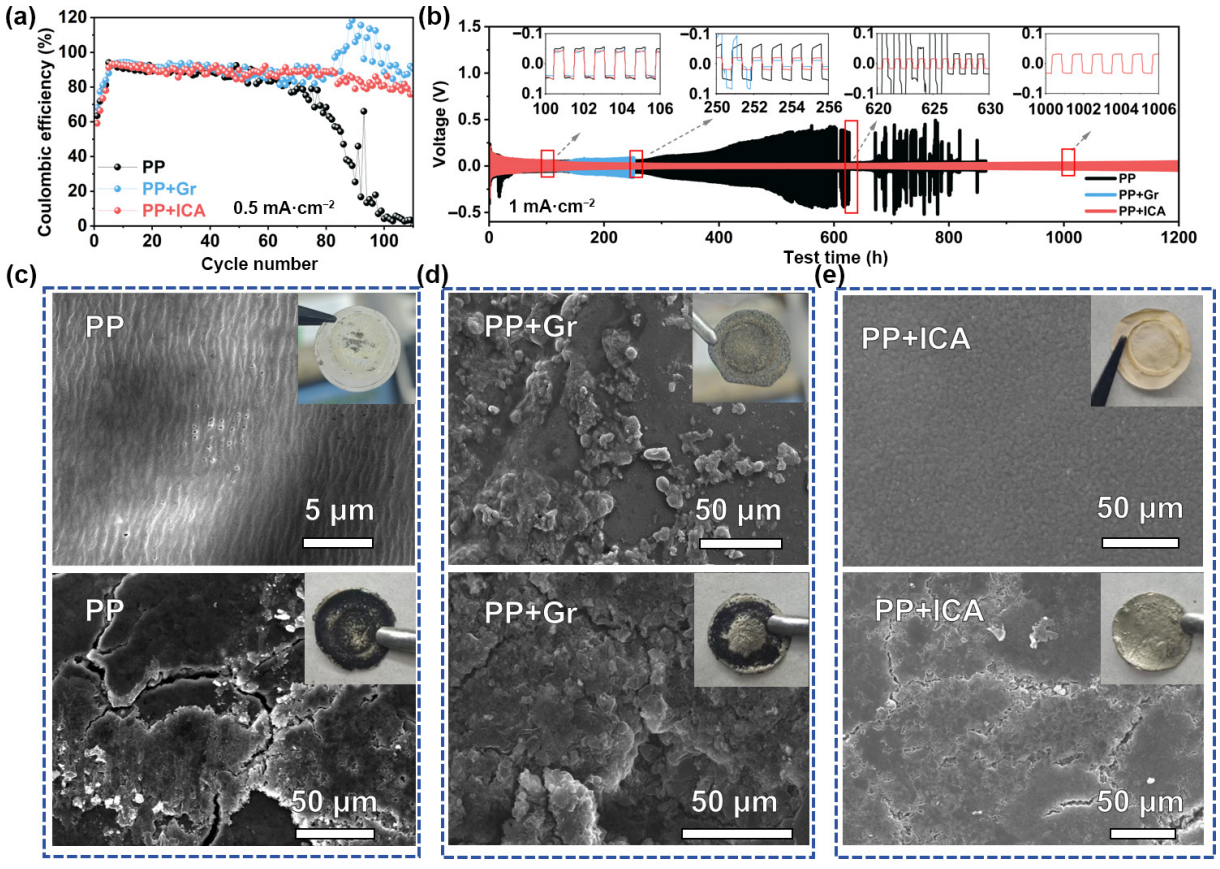

Figure 3 Lithium deposition behavior with different separators. (a) Coulombic efficiency of Li-Cu cells at 0.5 mA·cm^{-2}. (b) Voltage profiles of Li||Li symmetric cells at 1 mA·cm^{-2}. Insets show corresponding optical images after cycling. (c–e) SEM images of Li anodes and separators after cycling at current densities ranging from 0.5 to 2 mA·cm^{-2} using (c) PP, (d) PP+Gr, and (e) PP+ICA separators, demonstrating suppressed dendrite growth for PP+ICA.

high-rate conditions. The lithium deposition morphology and separator structure after cycling were examined to elucidate the origin of the electrochemical behavior. For the pristine PP separator, the lithium surface shows evident dead lithium accumulation and severe dendritic growth, accompanied by pore blockage of the cycled separator due to interfacial side reactions (Fig. 3(c)). The PP+Gr separator exhibits partial mitigation, but dead lithium and dendritic features are still observed, particularly near the electrode edge (Fig. 3(d)). In contrast, the PP+ICA separator maintains a smooth and dense lithium surface with suppressed dendrite formation (Fig. 3(e)). These observations confirm that ICA stabilizes lithium deposition and the separator interface during long-term cycling by establishing electrostatic repulsion against anions and solvent species and promoting selective Li^+ transport, thereby suppressing dendrite formation. No obvious delamination or cracking of the coating layer is observed after cycling, indicating good mechanical stability of the ICA coating.

Cycle life is a critical metric for evaluating the practical applicability of lithium batteries. To evaluate the practicality of PP+ICA, we assessed the cycle performance of LFP batteries at a rate of 1C (Fig. 4(a)). At the early stage of cycling (10th cycle), the Li||LFP cells with PP, PP+Gr, and PP+ICA separators deliver discharge capacities of 125, 127, and 141 mAh·g^{-1}, respectively, indicating that ICA modification enables more efficient Li^+ utilization from the initial cycles. After 1000 cycles, the PP+ICA battery still demonstrated a relatively high discharge specific capacity of 118.1 mAh·g^{-1}, resulting in a capacity retention rate of 81%. Conversely, the discharge specific capacity of LFP/PP/Li decreased to 83.9 mAh·g^{-1}, with a capacity retention rate of 63%. Throughout the cycling process, the voltage polarization value of PP+ICA remained stable (Fig. 4(b) and Fig. S13 in the ESM).

The rate capability of Li||LFP cells using different separators was further evaluated at current densities ranging from 0.1 to 3C (Fig. 4(c)). The average specific capacities of the PP+ICA battery exhibits the improved average specific capacities of at 0.1C, 0.5C, 1C, 2C, and 3C are 162.4, 149.5, 135.5, 122.8, and 111.6 mAh·g^{-1}, respectively, while retains a high reversible average specific capacity of 165 mAh·g^{-1} when reverted to 0.1C, In contrast, the PP and PP+Gr batteries show significantly declined capacities of 77.6 and 67.1 mAh·g^{-1} at 3C, respectively. This enhanced rate performance is attributed to the ICA-induced electrostatic field, which accelerates Li^+ migration and enables stable interfacial kinetics, thereby suppressing polarization under high current densities.

The electrochemical stability of the separator is critical for high-voltage cathode systems. As shown by linear sweep voltammetry (LSV) (Fig. S14 in the ESM), the PP+ICA separator remains electrochemically stable without evident oxidation below 4.5 V, satisfying the operational requirements of high-voltage NCM622 cathodes. The cycling performance of Li||NCM622 cells was subsequently evaluated at 1C (Fig. 4(d)). At the 10th cycle, the PP, PP+Gr, and PP+ICA cells deliver discharge capacities of 145, 166, and 170 mAh·g^{-1}, respectively, demonstrating improved initial kinetics and Li^+ transport in the presence of ICA. Upon extended cycling, the PP+ICA-based cell maintains a reversible capacity of 135.8 mAh·g^{-1} after 900 cycles, corresponding to a capacity retention of 80%. In comparison, the PP+Gr-based cell retains

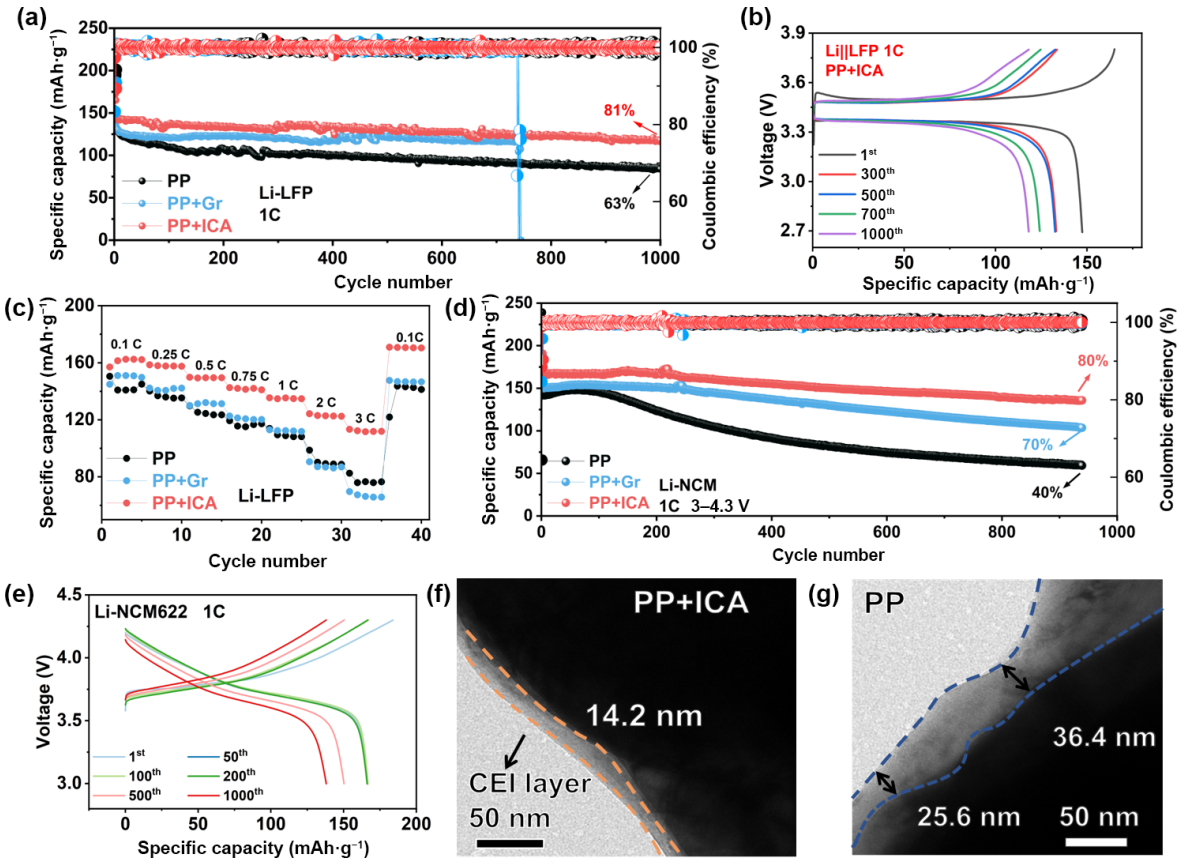

Figure 4 Electrochemical performance of full cells with different separators. (a) Long-term cycling performance of Li||LFP cells at 1C between 2.7–3.8 V. (b) Corresponding voltage profiles of Li||LFP cells with PP+ICA. (c) Rate performance of Li||LFP cells at different current densities (0.1C–3C). (d) Long-term cycling performance of Li||NCM622 cells at 1C between 3–4.3 V. (e) Corresponding voltage profiles of Li||NCM622 cells with PP+ICA. (f, g) TEM images of cathodes after cycling using PP+ICA and PP separators, showing the formation of a more uniform CEI layer in PP+ICA.

103.8 mAh·g^{-1} with a retention of 70%, while the PP-based cell suffers severe capacity decay to 59 mAh·g^{-1} with a retention of only 40%. The voltage profiles of the PP+ICA cell show a slow and stable increase in polarization during cycling, indicating that the ICA-induced electrostatic field effectively stabilizes interfacial charge transfer and Li^+ transport under high-voltage conditions (Fig. 4(e)). To further elucidate the interfacial characteristics, transmission electron microscopy (TEM) was performed on cycled NCM622 electrodes (Figs. 4(f) and 4(g)). It can be clearly seen that the cathode surface of the PP+ICA battery has a uniform cathode electrolyte interphase (CEI) layer with a thickness of only 14.2 nm. In contrast, the electrode cycled with a pristine PP separator shows a markedly thicker and non-uniform CEI layer, with local thicknesses exceeding 25.6 nm. The thinner and more homogeneous CEI formed in the presence of ICA indicates suppressed electrolyte decomposition and stabilized interfacial reactions, which contribute to reduced polarization growth and prolonged cycling stability in high-voltage lithium batteries.

Furthermore, the performance of single-layer pouch batteries (Si/C||NCM811) was investigated. As shown in Fig. 5(a), the pouch cell employing PP+ICA exhibits a slightly lower impedance than that using pristine PP, indicating improved interfacial ion transport enabled by the functional coating. At the 10th cycle, the PP and PP+ICA cells deliver discharge capacities of 125 and 150 mAh·g^{-1}, respectively. After 700 cycles at 1C, the PP+ICA battery retains a relatively high discharge specific capacity of 127 mAh·g^{-1}, with a capacity retention rate exceeding 80%. In contrast, the original PP battery exhibits a discharge specific capacity of only 104 mAh·g^{-1}, accompanied by a capacity retention rate of merely 64% (Fig. 5(b)). The practical functionality of the PP+ICA pouch cell is further demonstrated by its ability to continuously power LED lights (Fig. 5(c)). Consistent voltage profiles recorded at the 50th and 400th cycles show minimal variation, indicating low polarization and stable electrochemical behavior during long-term cycling (Fig. 5(d)). The interface conditions and gas behavior of pouch cells during the cycling process were examined using non-destructive ultrasonic imaging technology (Fig. 5(e)) [37]. Prior to cycling, it was clearly observed that the contact between the composite separator and the electrode was satisfactory. After 400 cycles, the PP+ICA pouch cell shows no noticeable interfacial degradation or gas accumulation, whereas slight gas generation is detected near the tab region in the PP-based cell. After 700 cycles, The PP+ICA pouch cell maintains stable interfacial contact with a more uniform ion transport pathway, and gas generation is limited to a small region (less than ~5%), whereas the PP-based cell shows extensive gas accumulation (~30%), indicating more severe side reactions without ICA modification. These results indicate that the ICA-induced electrostatic field stabilizes the interfacial ionic environment by suppressing anion and solvent participation in interfacial reactions, thereby reducing gas evolution and enabling durable cycling under practical conditions. The proposed electrostatic regulation mechanism is expected to be applicable to other conventional electrolyte systems, as it is mainly governed by ion–electrostatic interactions rather than specific solvent chemistry.

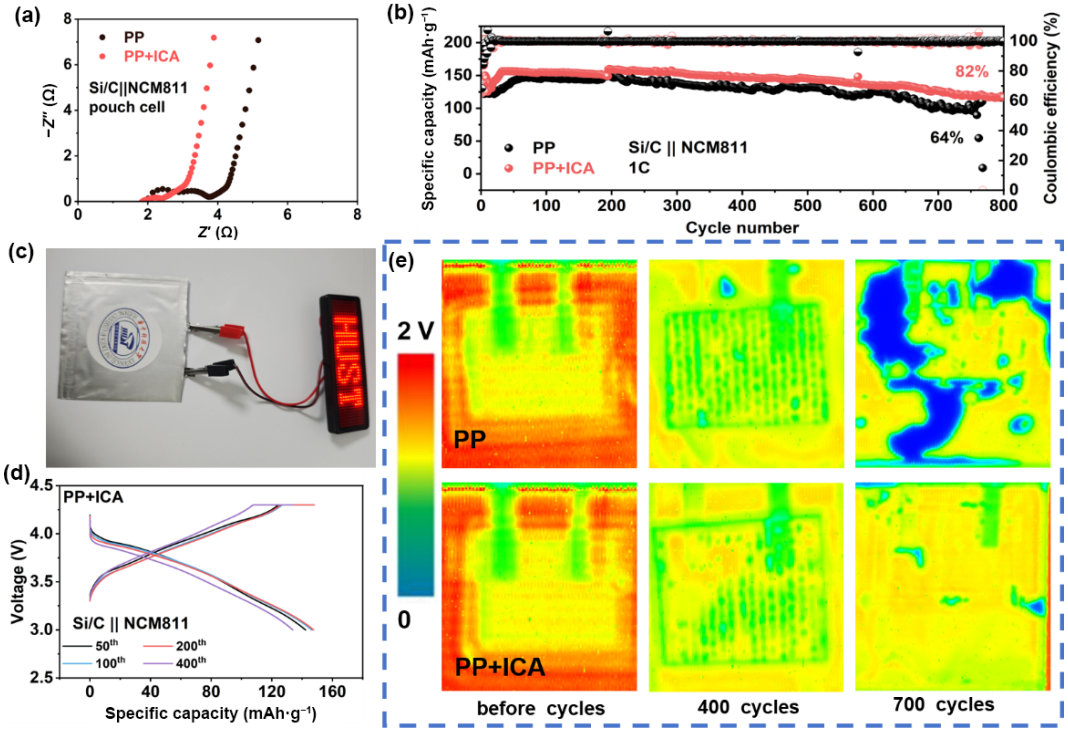

Figure 5 Electrochemical performance of pouch cells. (a) Electrochemical impedance spectra of pouch cells with PP and PP+ICA separators. (b) Long-term cycling performance of Si/C||NCM811 pouch cells at 1C. (c) Photograph of an LED powered by the pouch cell using PP+ICA. (d) Voltage profiles of the pouch cell during cycling. (e) Ultrasonic imaging of pouch cells at different cycling stages, showing suppressed gas generation and improved interfacial stability for PP+ICA.

3 Conclusion

In summary, this work addresses the interfacial limitations of commercial polypropylene separators through the development of sulfonic acid–grafted graphene (ICA) functionalized membranes. The immobilized sulfonate groups introduced by ICA generate a continuous anionic electrostatic field at the separator surface, which not only repels mobile PF_6^- anions but also excludes negatively polarized solvent molecules in the solvated environment. This dual electrostatic regulation weakens Li^+–solvent coordination, reduces the Li^+ desolvation energy barrier, and promotes Li^+-dominant charge transport across the interface. Consequently, the lithium-ion transference number is increased to 0.79 and the electrochemical stability window is extended to above 4.5 V. When applied in Li||NCM622 cells operated at a high cutoff voltage of 4.3 V, the PP+ICA separator delivers outstanding electrochemical performance, achieving a capacity retention of 82% after 1000 cycles at 1C with a Coulombic efficiency stably maintained above 99.5%. In addition, the fabrication process of the PP+ICA separator is compatible with existing manufacturing lines, and its effectiveness is further demonstrated in pouch-type power batteries, highlighting its strong potential for practical application and industrial implementation. The electrochemical performance achieved in this work is comparable to or better than that of many previously reported functional separators, demonstrating the effectiveness of the proposed electrostatic regulation strategy.

4 Experimental

4.1 Materials

Polyvinylidene difluoride (PVDF, $M_w \approx 150{,}000$) and N,N-dimethylformamide (DMF, 99%) were purchased from Aladdin Chemical Co., Ltd. (Shanghai, China). Commercial electrolyte (1 M $LiPF_6$ in EC/DEC, v/v = 1:1) was obtained from Kelode Experimental Equipment Technology Co., Ltd. (Dongguan, China). Polypropylene (PP) separators (Celgard 2325) and $LiFePO_4$ (LFP) cathode sheets for pouch cells were supplied by Guangdong Canrd New Energy Technology Co., Ltd. The ion-conducting agent (ICA) was provided by LiuGong Machinery Co., Ltd., and graphene (Gr) powder was purchased from Shenzhen Luckytong Industry Co., Ltd. All materials were used as received without further purification.

4.2 Preparation of PP+ICA separator

Functionalized separators were prepared by a solution-casting method. Typically, suspension with a solid content of approximately 0.3 wt.%, followed by ultrasonication for 2 h to obtain a homogeneous suspension. Subsequently, PVDF binder (5 wt.% relative to ICA) was added into the above suspension, and the mixture was magnetically stirred for 6 h to form a uniform coating slurry.

The slurry was coated onto one side of the PP separator at a coating speed of 5 cm·min^{-1}. The wet coating thickness was controlled at approximately 25 μm, resulting in a dry coating thickness of about 2–3 μm after solvent evaporation. The mass loading of ICA on the separator surface was determined to be approximately 0.3 mg·cm^{-2} (Fig. S14 in the ESM). The coated separators were dried at 60 °C for 12 h at vacuum to remove residual solvent and then punched into circular disks with a diameter of 19 mm. The resulting separators were denoted as PP+ICA. For comparison, graphene-coated separators (PP+Gr) were prepared following the same procedure.

To optimize the ICA loading, a series of separators with different ICA contents (0, 0.1, 0.2, 0.3, 0.5, and 1.0 wt.%) were fabricated and labeled as PP, PP+0.1%ICA, PP+0.2%ICA,

PP+0.3%ICA, PP+0.5%ICA, and PP+1%ICA, respectively. Electrochemical impedance and cycling tests revealed that the PP+0.1%ICA separator exhibited the lowest internal resistance and optimal electrochemical performance; therefore, this composition was selected for subsequent investigations unless otherwise specified. To optimize the coating amount, a series of ICA-coated separators with different ICA loadings (0–1.0 wt.%) were prepared and labeled as PP, PP+0.1%ICA, PP+0.2%ICA, PP+0.3%ICA, PP+0.5%ICA, and PP+1%ICA (Fig. S15 in the ESM). The electrolyte used in this work was 1 M $LiPF_6$ dissolved in a mixture of ethylene carbonate (EC) and diethyl carbonate (DEC) (1:1 by volume).

4.3 Preparation of LFP cathode

LFP cathodes were prepared by mixing LFP active material, Super P conductive carbon, and PVDF binder in a mass ratio of 8:1:1. PVDF (0.1 g) and Super P (0.1 g) were first dispersed in *N*-methyl-2-pyrrolidone (NMP) and stirred for 2 h, followed by the addition of LFP powder (0.8 g). The slurry was further stirred for 2 h to ensure homogeneity. The resulting slurry was cast onto aluminum foil using a doctor blade and vacuum-dried at 60 °C for 12 h. The dried electrodes were punched into disks with a diameter of 12 mm and stored in an argon-filled glovebox prior to cell assembly.

Acknowledgements

This work was supported by the National Key R&D Program of China (2023YFB2503801), National Natural Science Foundation of China (Grant No. 52302253), the Key Program of the National Natural Science Foundation of China (Grant No. 52231009). We thank the Analytical and Testing Centre of HUST and the State Key Laboratory of Materials Processing and Die & Mold Technology of HUST for XRD, SEM, Raman, and TEM measurements.

Declaration of conflicting interests

The authors declare no conflicting interests regarding the content of this article.

Data availability

All data needed to support the conclusions in the paper are presented in the manuscript and/or the Supplementary Materials. Additional data related to this paper may be requested from the corresponding author upon request.

Electronic Supplementary Material Supplementary material (Raman peak fitting analysis, additional morphological and elemental characterization, cross-sectional SEM images, thermal shrinkage evaluation, Raman and theoretical analysis of Li^+–solvent interactions, ionic conductivity and transference number measurements, supplementary electrochemical performance tests, and coating loading characterization) is available in the online version of this article at https://doi.org/10.26599/NRE.2026.9120239.

References

[1] Goodenough, J. B.; Park, K. S. The Li-ion rechargeable battery: A perspective. *J. Am. Chem. Soc.* **2013**, *135*, 1167–1176.
[2] Shahadat, M.; Khan, M. Z.; Rupani, P. F.; Embrandiri, A.; Sultana, S.; Ahammad, S. Z.; Wazed Ali, S.; Sreekrishnan, T. R. A critical review on the prospect of polyaniline-grafted biodegradable nanocomposite. *Adv. Colloid Interface Sci.* **2017**, *249*, 2–16.
[3] Zhu, M.; Tan, C. Y.; Fang, Q.; Gao, L.; Sui, G.; Yang, X. P. High performance and biodegradable skeleton material based on soy protein isolate for gel polymer electrolyte. *ACS Sustain. Chem. Eng.* **2016**, *4*, 4498–4505.
[4] Li, C. F.; Liu, S. H.; Shi, C. G.; Liang, G. H.; Lu, Z. T.; Fu, R. W.; Wu, D. C. Two-dimensional molecular brush-functionalized porous bilayer composite separators toward ultrastable high-current density lithium metal anodes. *Nat. Commun.* **2019**, *10*, 1363.
[5] Brand, M. J.; Hofmann, M. H.; Schuster, S. S.; Keil, P.; Jossen, A. The influence of current ripples on the lifetime of lithium-ion batteries. *IEEE Trans. Veh. Technol.* **2018**, *67*, 10438–10445.
[6] Xu, X. Q.; Cheng, X. B.; Jiang, F. N.; Yang, S. J.; Ren, D. S.; Shi, P.; Hsu, H.; Yuan, H.; Huang, J. Q.; Ouyang, M. G. et al. Dendrite-accelerated thermal runaway mechanisms of lithium metal pouch batteries. *SusMat* **2022**, *2*, 435–444.
[7] Li, M.; Lu, J.; Chen, Z. W.; Amine, K. 30 years of lithium-ion batteries. *Adv. Mater.* **2018**, *30*, 1800561.
[8] Liang, J.; Li, F.; Cheng, H. M. On energy: Batteries beyond lithium ion. *Energy Storage Mater.* **2017**, *7*, A1–A3.
[9] Liang, Y. R.; Zhao, C. Z.; Yuan, H.; Chen, Y.; Zhang, W. C.; Huang, J. Q.; Yu, D. S.; Liu, Y. L.; Titirici, M. M.; Chueh, Y. L. et al. A review of rechargeable batteries for portable electronic devices. *InfoMat* **2019**, *1*, 6–32.
[10] Yu, J. T.; Ma, X. Y.; Zou, X. Y.; Hu, Y.; Yang, M. C.; Cai, Y. L.; Yan, F. Regulated Li^+ solvation via competitive coordination mechanism of organic cations for high voltage and fast charging lithium metal batteries. *Angew. Chem., Int. Ed.* **2025**, *64*, e202416092.
[11] Cheng, X. B.; Zhang, R.; Zhao, C. Z.; Zhang, Q. Toward safe lithium metal anode in rechargeable batteries: A review. *Chem. Rev.* **2017**, *117*, 10403–10473.
[12] Wang, C. H.; Lu, W. J.; Lai, Q. Z.; Xu, P. C.; Zhang, H. M.; Li, X. F. A TiN nanorod array 3D hierarchical composite electrode for ultrahigh-power-density bromine-based flow batteries. *Adv. Mater.* **2019**, *31*, 1904690.
[13] Tikekar, M. D.; Choudhury, S.; Tu, Z. Y.; Archer, L. A. Design principles for electrolytes and interfaces for stable lithium-metal batteries. *Nat. Energy* **2016**, *1*, 16114.
[14] Wang, F. F.; Ke, X. Y.; Shen, K.; Zhu, L.; Yuan, C. A critical review on materials and fabrications of thermally stable separators for lithium-ion batteries. *Adv. Mater. Technol.* **2022**, *7*, 2100772.
[15] Lan, J.; Zhong, Y.; Peng, H.; Meng, Z. D.; He, N. X.; Lan, S. Z.; Huang, L.; Sun, S. G.; Deng, Y. P. Constructing an anion-capturing interface to achieve Li^+ cross-phase transport in composite solid electrolytes. *Nat. Commun.* **2026**, *17*, 376.
[16] Zhang, Y. H.; Du, S. B.; Pang, Y. F.; Gao, X. L.; Luo, D. W.; Xiang, X. Enhanced thermostability and electrochemical performance of separators based on an organic-inorganic composite binder composed of polyvinyl alcohol and inorganic phosphate for lithium ion batteries. *J. Alloys Compd.* **2022**, *895*, 162646.
[17] Lee, H.; Yanilmaz, M.; Toprakci, O.; Fu, K.; Zhang, X. W. A review of recent developments in membrane separators for rechargeable lithium-ion batteries. *Energy Environ. Sci.* **2014**, *7*, 3857–3886.
[18] Fan, Z. Y.; Zhang, J. W.; Wu, L. Q.; Yu, H. Q.; Li, J.; Li, K.; Zhao, Q. Solvation structure dependent ion transport and desolvation mechanism for fast-charging Li-ion batteries. *Chem. Sci.* **2024**, *15*, 17161–17172.
[19] Xu, R. N.; Wu, Y. R.; Dong, Z. Y.; Zheng, R. G.; Song, Z. S.; Wang, Z. Y.; Sun, H. Y.; Liu, Y. G.; Zhang, L. Halide solid electrolytes in all-solid-state batteries: Ion transport kinetics, failure mechanisms and improvement strategies. *Nano Energy* **2024**, *132*, 110435.
[20] Wen, J. Y.; Dai, Y. M.; Yu, Q.; Ouyang, Z. Y.; Luo, W.; Huang, Y. H. Promise and perspectives of garnet-based anode-free solid-state batteries. *Acc. Mater. Res.* **2025**, *6*, 902–913.

[21] Fan, Z. X.; Chen, X. Y.; Shi, J. J.; Nie, H.; Zhang, X. M.; Zhou, X. P.; Xie, X. L.; Xue, Z. G. Functionalized separators boosting electrochemical performances for lithium batteries. *Nano-Micro Lett.* **2025**, *17*, 128.
[22] Ren, W. C.; Zheng, Y. N.; Cui, Z. H.; Tao, Y. S.; Li, B. X.; Wang, W. T. Recent progress of functional separators in dendrite inhibition for lithium metal batteries. *Energy Storage Mater.* **2021**, *35*, 157–168.
[23] Li, J. Q.; Chen, L.; Wang, F. L.; Qin, Z. Y.; Zhang, Y.; Zhang, N.; Liu, X. H.; Chen, G. Anionic metal-organic framework modified separator boosting efficient Li-ion transport. *Chem. Eng. J.* **2023**, *451*, 138536.
[24] Hu, Y. T.; Wang, C. J.; Wu, Y.; Zhao, Q.; Li, A.; Zhang, Q. Q.; Liu, J. B.; Jin, Y. H.; Wang, H. Negatively charged separators facilitating lithium-ion conduction to stabilize lithium metal anodes. *J. Mater. Chem. A* **2023**, *11*, 12052–12061.
[25] He, C. N.; Wang, H. Y.; Wang, L. L.; Xue, S. Anionic/cationic grafted silica modified separator boosting efficient Li-ion transport. *Prog. Org. Coat.* **2025**, *207*, 109398.
[26] Liu, Y.; Hou, T. Y.; Zhang, W.; Gou, B.; Li, F. Q.; Wang, H. N.; Deng, X.; Li, D. G.; Xu, H. H.; Huang, Y. H. Anion-repulsive polyoxometalate@MOF-modified separators for dendrite-free and high-rate lithium batteries. *Interdiscip. Mater.* **2025**, *4*, 190–200.
[27] Liu, Y. J.; Tao, X. Y.; Wang, Y.; Jiang, C.; Ma, C.; Sheng, O. W.; Lu, G. X.; Lou, X. W. Self-assembled monolayers direct a LiF-rich interphase toward long-life lithium metal batteries. *Science* **2022**, *375*, 739–745.
[28] Liao, S. J.; Cheng, D. M.; Xu, X. Y.; Li, Q. Y.; Xu, S. Z.; Zhang, J. C.; Wei, H. L.; Wei, Y.; Li, Q.; Li, K. et al. SO_3Li-grafted ion-conducting agents for graphite-based lithium-ion batteries with extended cycle life. *Chin. Chem. Lett.* **2026**, *37*, 111329.
[29] Wang, X.; Luo, Z. C.; Huang, J. T.; Chen, Z.; Xiang, T.; Feng, Z. J.; Wang, J.; Wang, S. N.; Ma, Y. C.; Yang, H. Y. et al. S/N-co-doped graphite nanosheets exfoliated via three-roll milling for high-performance sodium/potassium ion batteries. *J. Mater. Sci. Technol.* **2023**, *147*, 47–55.
[30] Naren, T.; Jiang, R. H.; Qing, P.; Huang, S. Z.; Ling, C. H.; Lin, J. L.; Wei, W. F.; Ji, X. B.; Chen, Y. J.; Zhang, Q. C. et al. Stabilizing lithium metal batteries by synergistic effect of high ionic transfer separator and lithium-boron composite material anode. *ACS Nano* **2023**, *17*, 20315–20324.
[31] Miao, X.; Song, C. X.; Hu, W.; Ren, Y. Y.; Shen, Y.; Nan, C. W. Achieving high-performance lithium-sulfur batteries by modulating Li^+ desolvation barrier with liquid crystal polymers. *Adv. Mater.* **2024**, *36*, 2401473.
[32] Kong, Y.; Qiu, X. M.; Xue, Y. R.; Li, G. X.; Qi, L.; Yang, W. L.; Liu, T. F.; Li, Y. L. Sulfonic acid-functionalized graphdiyne for effective Li–S battery separators. *J. Am. Chem. Soc.* **2024**, *146*, 23764–23774.
[33] Bai, P.; Li, J.; Brushett, F. R.; Bazant, M. Z. Transition of lithium growth mechanisms in liquid electrolytes. *Energy Environ. Sci.* **2016**, *9*, 3221–3229.
[34] Liu, J.; Zhang, J. P.; Zhu, J.; Zhao, R. Q.; Zhang, Y. M.; Ma, Y. F.; Li, C. X.; Zhang, H. T.; Chen, Y. S. A lithium sulfonylimide COF-modified separator for high-performance Li–S batteries. *Nano Res.* **2023**, *16*, 12601–12607.
[35] Wang, K.; Zhao, T.; Lv, R. X.; Tang, W. M.; Yu, T. Y.; Chen, G. S.; Li, L.; Wu, F.; Chen, R. J. Dendrite-free lithium-metal batteries enabled by 2D lithophilic conjugated polymer on separator. *Adv. Energy Mater.* **2024**, *14*, 2401281.
[36] Kong, Y.; Ao, X.; Huang, X.; Bai, J. L.; Zhao, S. Q.; Zhang, J. Y.; Tian, B. B. Ni–CeO_2 heterostructures in Li–S batteries: A balancing act between adsorption and catalytic conversion of polysulfide. *Adv. Sci.* **2022**, *9*, 2105538.
[37] Deng, Z.; Huang, Z. Y.; Shen, Y.; Huang, Y. H.; Ding, H.; Luscombe, A.; Johnson, M.; Harlow, J. E.; Gauthier, R.; Dahn, J. R. Ultrasonic scanning to observe wetting and "Unwetting" in Li-ion pouch cells. *Joule* **2020**, *4*, 2017–2029.

Yuanyuan Luo received her B.S. degree from the School of Materials Science and Engineering, Huazhong University of Science and Technology, Wuhan, China, and is currently pursuing her M.S. degree at the same institution. She is currently a postgraduate student under the supervision of Prof. Henghui Xu. Her research focuses on separator modification and solid-state electrolytes for lithium-based energy storage systems.

Henghui Xu is a professor at Huazhong University of Science and Technology, China. He received his Ph.D. in 2015 and conducted research at The University of Texas at Austin. His research focuses on lithium-ion and solid-state batteries. He has published over 100 SCI papers with more than 10,000 citations.